Bifurcation Analysis of Nose Landing Gear Shimmy with Lateral and Longitudinal Bending

Phanikrishna Thota* Bernd Krauskopf*

Mark Lowenberg†

Faculty of Engineering, University of Bristol, Bristol BS8 1TR, United Kingdom

We develop and study a model of an aircraft nose landing gear with torsional, lateral and longitudinal degrees of freedom. The corresponding three modes are coupled in a nonlinear fashion via the geometry of the landing gear in the presence of a nonzero rake angle, as well as via the nonlinear tyre forces. Their interplay may lead to different types of shimmy oscillations as a function of the forward velocity and the vertical force on the landing gear. Methods from nonlinear dynamics, especially numerical continuation of equilibria and periodic solutions, are used to asses how the three modes contribute to different types of shimmy dynamics. We conclude that the longitudinal mode does not actively participate in the nose landing gear dynamics over the entire range of forward velocity and vertical force.

I. Introduction

Unwanted oscillations in wheeled vehicles — generally referred to as shimmy oscillations — can be caused by a variety of factors, such as component flexibilities, freeplay, etc.[1–4] Even though the triggering mechanism for shimmy oscillations may vary in different types of vehicles, the consequences of such oscillations are wear and tear of components and discomfort to the riders. Specifically, in the case of aircraft landing gears, considered here, extreme shimmy oscillations can result in high maintenance costs, and also in violent vibrations in the cockpit, sometimes even restricting the pilot's ability to read the instrument panel.

Efforts to study shimmy oscillations, initially in cars, date back to the early 1900's. As entry points to the literature see, for example, the surveys by Dengler *et al.*,[5] Smiley[6] and Pritchard,[7] who discuss theoretical as well as experimental studies, stressing both tyre theories and structural aspects of shimmy oscillations. Broulhiet's[8] seminal work on the effect of side slip of an elastic tyre on shimmy oscillations forms the basis for many modern shimmy studies. However, it was von Schlippe and Dietrich[9] who developed one of the earliest and still widely used models — the *stretched string model* of tyre kinematics — and used it for shimmy analysis of an aircraft landing gear. Smiley[6] studied shimmy oscillations in aircraft for three different landing gear structures and studied them by means of linear stability analysis. Furthermore, he provided a comprehensive comparison of different tyre models. Even though one of the landing gears Smiley considered included a nonzero rake angle, its nonlinear and geometric effects were not considered in his analysis. More recently Somieski[10] performed time domain analysis of a set of nonlinear ordinary differential equations representing a nose landing gear. He reported that stable shimmy oscillations appear (and disappear) via a Hopf bifurcation[11,12] and exist over a range of velocities of the aircraft. A different approach was taken by Woerner and Noel[13] who studied shimmy oscillations by frequency analysis. They described the main cause of shimmy oscillations as the energy transfer from the contact force between the tyres and the ground to vibrational modes of the landing gear. In particular, Woerner and Noel studied the dependence of frequency on the swivel friction and forward velocity; this suggested that coupled motion may occur due to resonance phenomena when the forward velocity changes, a mechanism that may lead to high-amplitude shimmy oscillations.

*Department of Engineering Mathematics

†Department of Aerospace Engineering

In this paper we study the onset and stability of shimmy oscillations in an aircraft nose landing gear in a free rolling scenario with emphasis on the influence of different vibrational modes on the landing gear dynamics. We consider here the main three vibrational modes of a generic midsize commercial passenger aircraft, which are: the torsional mode corresponding to the rotation about the gear strut axis, the lateral bending mode that is representative of vibrations of the gear from left to right, and the longitudinal bending mode in the direction of straight-line travel of the aircraft. These modes of vibration are coupled via the geometry of the gear and via the force generated at the tyre-ground contact. Their nonlinear interaction plays an important role in aircraft shimmy dynamics. Note that we do not consider the vertical mode associated with the oleos (shock dampers) of the gear. Even though some of the earlier works[5] on aircraft shimmy oscillations reported that the vertical mode may be excited due to rough runways, this is not generally the case on today's smooth runways.

Specifically, we develop and study a seven-dimensional ordinary differential equation model for the torsional, lateral and longitudinal modes and the tyre force. In a first-order approximation each vibrational mode is modeled as a single degree of freedom oscillator, which is coupled with the other modes via the gear geometry and the tyre-ground contact. The elastic tyre is modeled by a modified version of the stretched string model[9] that includes the effect of the lateral bending mode on the deformation of the tyre. Importantly, we consider the case of a nonzero rake angle of the gear, which has consequences for the coupling of the modes via nonlinear geometric effects.

The model presented here is an extension of a five-dimensional model that we developed previously,[14] which does not include the longitudinal degree of freedom, but allowed for the nonlinear interaction between the torsional and lateral modes in an aircraft nose landing gear. This made it possible to identify types of shimmy oscillations that are dominated either by the torsional mode, the lateral mode, or transient behaviour featuring contributions from both. In the latter case one may find quasiperiodic shimmy oscillations, which is characterized by two incommensurate frequencies.[11,12] We remark that stable quasiperiodic shimmy oscillations have been found by Pacejka[15] in the quite different setting of a pulled trailer with zero rake angle and negligible damping.

The main question that we address is whether the inclusion of the longitudinal mode affects the dynamics in a significant way. To answer this question we perform time and frequency domain analysis of the different types of shimmy oscillations with MATLAB, in conjunction with a numerical bifurcation analysis with the software package AUTO.[17] This allows us to assess the role of the longitudinal mode over the entire relevant operational range of forward velocity of the aircraft and vertical force on the gear by means of one- and two-parameter bifurcation diagrams. We also investigate how regions of different types of shimmy oscillations in the two-parameter bifurcation diagrams change with the damping in the torsional mode.

The paper is organized as follows. Section II introduces and discusses the mathematical model of the nose landing gear. Section III is devoted to the analysis of the model, where we show representative time series and frequency spectra, one-parameter continuations in the forward velocity, and a two-parameter bifurcation diagram in the plane of forward velocity and vertical force on the gear. Section IV investigates the influence of torsional damping on the bifurcation diagrams. Finally, Sec. V summarizes and discusses directions of future research.

II. Model of a nose landing gear

The nose landing gear of an aircraft as considered here is shown in Fig. 1. A wheel with pneumatic tyre of radius R is mounted on an axle that is connected to a strut via a mechanical caster (trail) of length e. The combined effect of the fuselage and wings is modeled as a block of mass that exerts a vertical force F_z on the gear while moving with a forward velocity V. We use one of the conventionally accepted coordinate systems for aircraft analysis, where the positive X-axis is along the fuselage centerline, and points in the backward direction of the aircraft, the Z-axis is the upward normal to the flat ground, and the Y-axis completes the right-handed coordinate system. In the static equilibrium position of the gear, the strut axis lies in the (X, Z)-plane, and it is inclined to the vertical at a rake angle ϕ. Note that the rake angle varies significantly from one aircraft type to the other and may be anywhere in the range of 0–30 degrees, while a range of 0–15 degrees is more typical for commercial passenger aircraft.

We consider here a nose landing gear with three geometrical degrees of freedom. First, the gear may rotate about the strut axis S, which gives rise to the *torsional mode* described by the torsion angle ψ (rad). Second, the gear may bend about the X-axis, which gives rise to the *lateral mode*. It is described in a

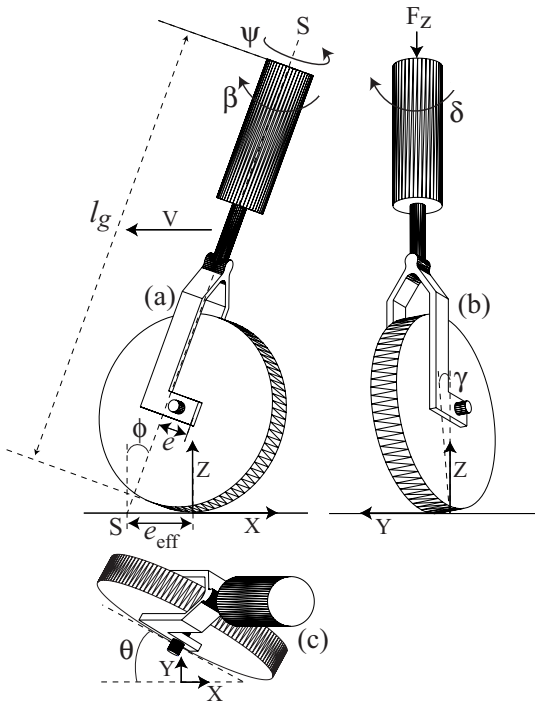

Figure 1. Schematic side (a), front (b) and top (c) views of an aircraft nose landing gear.

first-order approach by the angle δ (rad) over which the strut is rotated about the mount point in the lateral direction. Third, the gear may bend about the Y-axis, which gives rise to the *longitudinal mode* as described by the angle β (rad) over which the strut is rotated in the longitudinal direction. The model considered here is an extension of the nose landing gear model presented in Thota *et al.*[14] Specifically, we add the extra degree of freedom corresponding to the longitudinal motion as described by β to investigate its influence on the overall dynamics.

The longitudinal mode is coupled to the torsional and lateral modes via the tyre-ground interface, but also induces several geometrical effects into the gear dynamics. Namely, the angle β contributes to the overall rake angle, so that we are dealing with an effective rake angle of $(\phi+\beta)$. The effective rake angle in turn has several geometric consequences. First of all, the effective caster length e_{eff}, which has significant influence on the stability of the gear,[14,18] now takes the form

$$e_{\text{eff}} = e\cos(\phi+\beta) + R\tan(\phi+\beta) + e\sin(\phi+\beta)\tan(\phi+\beta)\,. \tag{1}$$

Hence, any longitudinal bending motion induces a time-varying effective caster length e_{eff}, while e_{eff} is constant when the longitudinal bending mode is not taken into account (that is, $\beta \equiv 0$).

Apart from influencing the effective caster length, there are other geometrical effects of a nonzero effective rake angle. Specifically, the swivel angle θ, which is the angle between the wheel center plane and the X−axis, is related to the torsion angle ψ by

$$\theta = \psi\ \cos(\phi+\beta)\,. \tag{2}$$

Furthermore, for a nonzero torsion angle ψ, a tilt γ in the wheel center plane is created; it is given by

$$\gamma = \psi\sin(\phi+\beta)\,. \tag{3}$$

Finally, a nonzero effective rake angle changes the moment that destabilizes the static orientation of the gear.[14]

Equations (1)–(3) contribute to the coupling of the longitudinal mode (that is, β) to the other two modes, described by ψ and δ. This type of pure geometrical coupling is an addition to the dynamic coupling between the modes via the forces generated at the tyre-ground contact of the elastic tyre. We use a modified version of the well-established stretched string tyre model developed by von Schlippe and Dietrich.[9] Our modification

Table 1. System parameters and their values as used in the modeling.

symbol	parameter	value	
	structure parameters		
l_g	gear height	2.5	m
e	caster length	0.16	m
ϕ	rake angle	14.7	deg (0.2571 rad)
k_ψ	torsional stiffness of strut	3.0 x 10^5	N m rad^{-1}
k_δ	lateral bending stiffness of strut	3.24 x 10^6	N m rad^{-1}
k_β	longitudinal bending stiffness of strut	3.0 x 10^7	N m rad^{-1}
c_ψ	torsional damping of strut	110.0	N m s rad^{-1}
c_δ	lateral bending damping of strut	1.0	N m s rad^{-1}
c_β	longitudinal bending damping of strut	10.0	N m s rad^{-1}
I_z	moment of inertia of strut w.r.t Z-axis	100.0	kg m^2
I_y	moment of inertia of strut w.r.t Y-axis	300.0	kg m^2
I_x	moment of inertia of strut w.r.t X-axis	600.0	kg m^2
	tyre parameters		
R	radius of nose wheel	0.362	m
h	contact patch length	0.1	m
k_α	self-aligning coefficient of elastic tyre	1.0	m/rad
k_λ	restoring coefficient of elastic tyre	0.01	rad^{-1}
c_λ	damping coefficient of elastic tyre	570.0	N m^{2}rad^{-1}
L	relaxation length	0.3	m
α_m	self-aligning moment limit	10.0	deg (0.1745 rad)
	continuation parameters		
F_z	vertical force on the gear	40.0-200.0	kN
V	forward velocity	0.0-110.0	m s^{-1}

includes the effect of the lateral deformation caused by the lateral bending mode δ. Since the tilt γ is known to influence tyre dynamics in cars more than in aircraft,[14] we do not model its effect here.

Overall, the equations of motion for the nose landing gear model can be written as

$$I_z\ \ddot{\psi} + M_{K_\psi} + M_{D_\psi} + M_{F_1} + M_{D_\alpha} - F_z\ \sin(\phi+\beta)\ e_{\text{eff}}\ \sin(\theta) \;=\; 0, \tag{4}$$

$$I_x\ \ddot{\delta} + M_{K_\delta} + M_{D_\delta} + M_{\lambda_\delta} - F_z\ e_{\text{eff}}\ \sin(\theta) \;=\; 0, \tag{5}$$

$$I_y\ \ddot{\beta} + M_{K_\beta} + M_{D_\beta} + M_{\lambda_\beta} - F_z\ l_g\ \sin(\phi+\beta) \;=\; 0, \tag{6}$$

$$\dot{\lambda} + \frac{V}{L}\lambda - V\ \sin(\theta) - l_g\ \dot{\delta}\ \cos(\delta) - (e_{\text{eff}} - h)\ \cos(\theta)\ \dot{\psi}\ \cos(\phi+\beta) \;=\; 0. \tag{7}$$

Equations (4)–(7) are a seven-dimensional model for the dynamics of the nose landing gear. Here Eq. (4), Eq. (5) and Eq. (6) model the torsional, lateral and longitudinal degrees of freedom, with moments of inertia I_z, I_x and I_y, respectively. Equation (7) comes from von Schlippe's stretched string model,[9] which describes the nonlinear kinematic relationship between the torsion angle ψ, lateral bending angle δ and the lateral deformation λ of the leading edge of the contact patch of the tyre. Note that the torsional mode and the lateral bending mode appear as part of a five-dimensional model,[14] but Eq. (6) and the respective coupling terms are new. To keep this paper self-contained we now present a more detailed description of the individual terms of Eqs. (4)–(7).

The second and third terms in Eq. (4) describe the stiffness and damping of the torsional mode as $M_{K_\psi} = k_\psi\psi$ and $M_{D_\psi} = c_\psi\psi$. The second and third terms in Equations (5)–(6) describe the stiffness and damping of the lateral and longitudinal modes in exactly the same way; see Table 1 for the values of the

stiffnesses k_* and dampings c_* of the three modes as used in our calculations. The equations also contain coupling moments generated due to the interaction of the elastic tyre with the ground. Specifically, the tyre force F_{K_λ}, which is a result of the tyre deformation λ, tries to restore the motions to their equilibrium states and simultaneously acts as a coupling factor for the three modes.

II.A. Coupling of the torsional mode

In Eq. (4), the combined moment M_{F_1} due to the tyre's restoring force F_{K_λ} and self-aligning moment M_{K_α} is given by

$$M_{F_1} = M_{K_\alpha} + e_{\text{eff}}\ F_{K_\lambda}. \tag{8}$$

Here M_{K_α} is given by the piecewise continuous function[10,14]

$$M_{K_\alpha} \quad = \quad \begin{cases} k_\alpha \frac{\alpha_m}{\pi} \sin\left(\alpha \frac{\pi}{\alpha_m}\right)\ F_z & \text{if } |\alpha| \le \alpha_m, \\ 0 & \text{if } |\alpha| > \alpha_m, \end{cases} \tag{9}$$

and the lateral restoring force F_{K_λ} due to tyre deformation is given by

$$F_{K_\lambda} = k_\lambda \quad \tan^{-1}\left(7.0\ \tan\left(\alpha\right)\right)\ \cos\left(0.95\ \tan^{-1}\left(7.0\ \tan\left(\alpha\right)\right)\right)\ F_z. \tag{10}$$

The constants k_α and k_λ represent the torsional and lateral stiffness coefficients of the tyre. The slip angle α is related to the lateral deformation λ by $\alpha = \tan^{-1}(\lambda/L)$, where L is the relaxation length of the tyre. In this work we consider a piecewise smooth approximation to the self-aligning moment M_{K_α}; the constant α_m in Eq. (9) sets a limit on the slip angle α beyond which M_{K_α} is taken to be zero.

Finally, in Eq. (4) the moment M_{D_α} due to the tyre's tread damping is given by

$$M_{D_\alpha} = c_\lambda\ \cos\left(\phi + \beta\right) \frac{\dot{\psi}}{V}. \tag{11}$$

It is clear from the above equations, describing the influence of the tyre-ground contact, that the longitudinal mode variable β enters into the torsional mode via the effective caster length e_{eff}, and also via the last term in Eq. (4) representing a destabilizing moment.

II.B. Coupling of lateral and longitudinal modes

In Eq. (5) the moment M_{λ_δ} couples the torsional, lateral and longitudinal motions; it is given by

$$M_{\lambda_\delta} = l_g\ F_{K_\lambda}\ \cos(\theta)\ \cos(\phi + \beta), \tag{12}$$

where l_g is the distance between the point of attachment of the gear to the fuselage and the ground. The last term in Eq. (5) represents a destabilizing moment that is proportional to the vertical load on the aircraft. This moment becomes active in a significant way during landing of an aircraft, when there is a sudden increase in the vertical load.

Similarly, in Eq. (6) the coupling moment M_{λ_β} is given by

$$M_{\lambda_\beta} = l_g\ F_{K_\lambda}\ \sin(\theta)\ \cos\left(\phi + \beta\right). \tag{13}$$

Again, the last term in Eq. (6) represents a destabilizing moment proportional to the vertical force F_z as well as to the sine of the effective rake angle. For a nonzero rake angle ϕ of the landing gear this moment is responsible for a nonzero stable equilibrium position. This is different from the case when the longitudinal degree of freedom β is not considered in the model, so that the equilibrium position is at zero.[14]

II.C. Tyre kinematics

Equation (7) describes the motion of the tyre under the influence of the strut's torsional, lateral and longitudinal motions. Here, the resultant tyre deformation is an algebraic sum of the deformation caused by the torsional and lateral modes. We incorporate into Eq. (7) the effect of the lateral deformation caused due to the lateral bending mode[14] by adding an extra term to the conventional equation representing the stretched string model.[9] The superimposing of the effects of both the modes is justified by derivations that are not presented here. The longitudinal mode variable β enters into the tyre motion via the effective caster length e_{eff} and the effective rake angle.

III. Nonlinear dynamics of the nose landing gear

We now consider the nonlinear dynamics of mathematical model (4)–(7) of the nose landing gear. To this end we set the parameters as summarized in Table 1, which are realistic choices for a generic midsized passenger aircraft. First, we present a time and frequency domain analysis of the model with MATLAB for three different settings of the forward velocity V and the downward force F_z, which correspond to three different kinds of shimmy oscillations. This allows us to investigate the relative contributions of the three vibrational modes to the overall landing gear dynamics. Next, we present a one-parameter bifurcation study in the forward velocity V to determine the relative strengths of the three modes over a larger range of operating conditions. Finally, we present a direct comparison of two-parameter bifurcation diagrams in the (V, F_z)-plane of Eqs. (4)–(7), with and without an active longitudinal bending mode. The bifurcation studies were performed with the numerical continuation package AUTO,[16] which allows one to follow equilibria and periodic solutions, and their bifurcations in system parameters.

III.A. Time and frequency domain analysis

For the parameter values in Table 1 the linear damped natural frequencies of the torsional, lateral and longitudinal modes in the case of an unloaded gear are 8.71 Hz, 11.69 Hz and 50.32 Hz, respectively. These frequencies of the uncoupled linear modes are in realistic ranges for a midsize passenger aircraft. Due to the nonlinearities of the model, the frequencies of the three modes during shimmy oscillations will deviate somewhat from their natural frequencies, but they remain clearly distinguishable.

The lateral and longitudinal bending modes manifest themselves at the tyre-ground interface as motions that deform the tyre. Therefore, it is convenient to consider not the angular variables δ and β themselves, but their *strokes* at ground level as given by

$$\delta^* = l_g \ \sin(\delta) \quad \text{and} \quad \beta^* = l_g \ \sin(\beta), \tag{14}$$

where l_g is the height of the gear. The strokes δ^* and β^* allow for a direct comparison of the amplitudes of the lateral and longitudinal motions relative to the tyre deformation λ (measured in meters). Since all modes interact via the tyre, the respective frequency components in the power spectrum of λ reveal the contributions of the three modes to the dynamics. To assess the role of the longitudinal bending oscillations we consider the power spectrum of β^* as well.

Figure 2 shows time histories and frequency spectra for three different sets of values of the velocity V and the vertical force F_z. Each group of panels (a) to (c) illustrates the relative contributions of the different modes to different kinds of shimmy oscillations. Three time series panels (left column) show oscillations of the torsion angle ψ, of the tyre deformation λ in comparison with the lateral stroke δ^*, and of the longitudinal stroke β^*, respectively. Notice the difference in scale, which shows that the longitudinal stroke β^* oscillates with negligible amplitudes, while the lateral stroke δ^* oscillates with amplitudes of several centimeters. The two spectra panels (right column) show the frequency content of the tyre deformation λ, and of the longitudinal stroke β^*.

Figure 2(a1)–(a5) shows shimmy oscillations for $V = 20$ m/s and $F_z = 60$ kN, a relatively low velocity and low vertical force. This type of shimmy dynamics can be identified as pure torsional shimmy: ψ oscillates with a considerable amplitude of about 7 degrees, and this induces oscillations of the tyre deformation λ [Fig. 2(a1) and (a2)] at the frequency $f_t \approx 8.79$ Hz of the torsional mode [Fig. 2(a4)]. The lateral mode is effectively following this excitation with very small amplitude. However, the longitudinal mode is oscillating at the frequency $f_\beta \approx 49.8$ Hz and with negligible amplitudes. Even though the stiffness in the longitudinal mode is slightly higher than in the lateral and torsional mode, the restoring effect of the coupling term M_{λ_β} extracts most of the energy out of the longitudinal mode.

For the higher-vertical force case of $V = 5$ m/s and $F_z = 162$ kN in Fig. 2(b1)–(b5), we find a very different type of shimmy oscillations: pure lateral shimmy driving the torsional mode. Here, the lateral mode drives the tyre deformation at a comparable amplitude of about 5 cm [Fig. 2(b2) and (b4)] and at a frequency $f_l \approx 11.72$ Hz. In contrast to the earlier case, the torsional mode follows this excitation by the lateral mode. Again, the longitudinal mode is oscillating with an extremely low amplitude about a nonzero equilibrium and with frequency $f_\beta \approx 49.8$ Hz.

A qualitatively different type of shimmy dynamics can be seen in Fig. 2(c1)–(c5) for $V = 12$ m/s and $F_z = 162$ kN, where we see an interaction between the torsional mode and the lateral bending mode. In Fig. 2(c1) and (c2), the modulation in the amplitudes of the torsional and lateral bending modes indicates an interplay

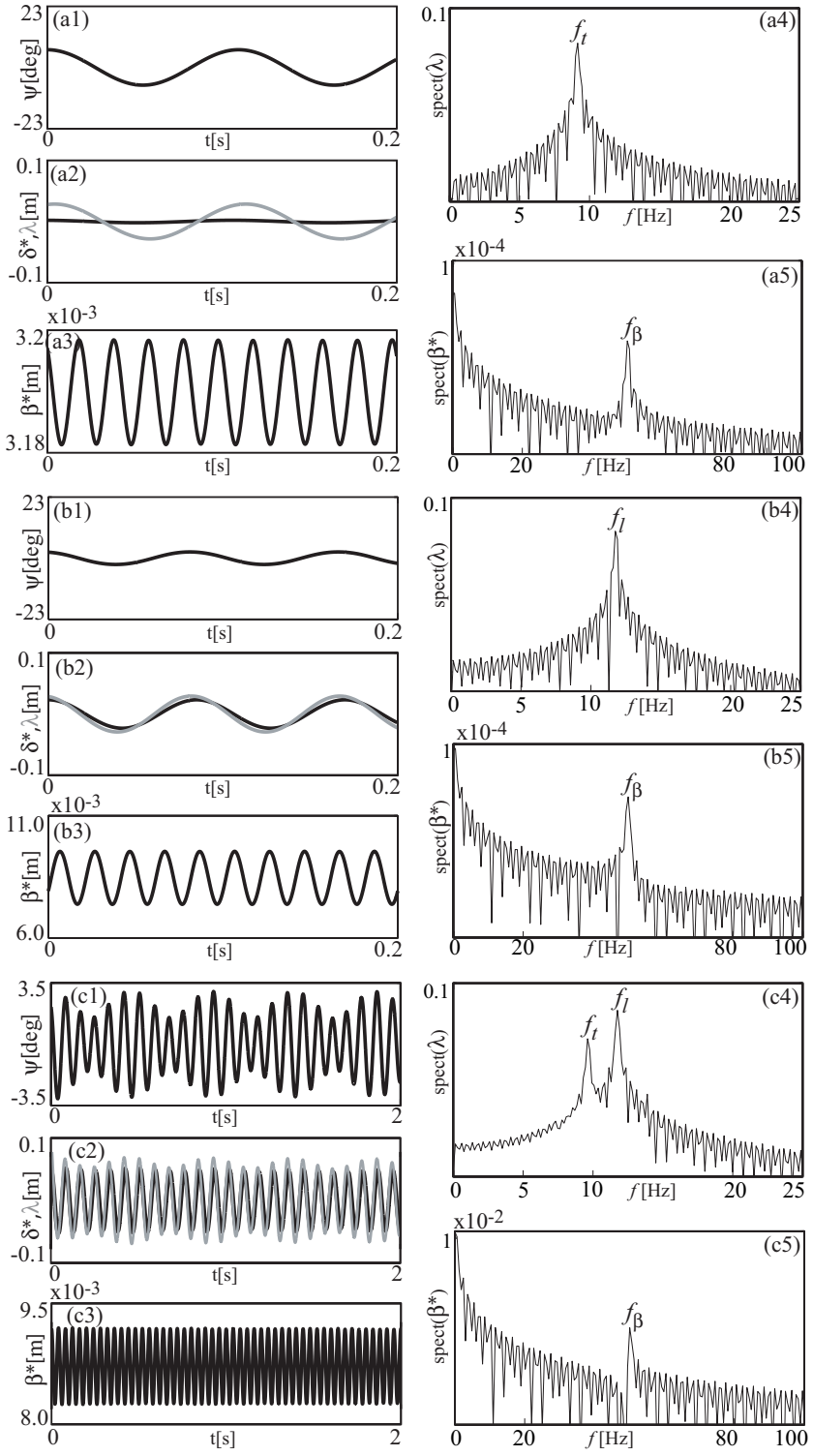

Figure 2. Time histories (left column) and frequency spectra (right column) for $V = 20$ m/s and $F_z = 60$ kN (a), for $V = 5$ m/s and $F_z = 162$ kN (b), and for $V = 12$ m/s and $F_z = 162$ kN (c). The individual panels for each case (a) to (c) show time series of the torsional mode variable ψ, of the lateral stroke δ^* (black) and the tyre deformation λ (grey), and of the longitudinal stroke β^*, as well as spectra of the tyre deformation λ and of the longitudinal stroke β^*; f_t, f_l and f_β indicate the frequencies of the torsional, lateral and longitudinal modes.

of two *incommensurate* frequencies. The frequency spectrum given in Fig. 2(c4) clearly shows that these two frequencies correspond to the torsional (f_t) and lateral bending (f_l) modes. The time histories shown

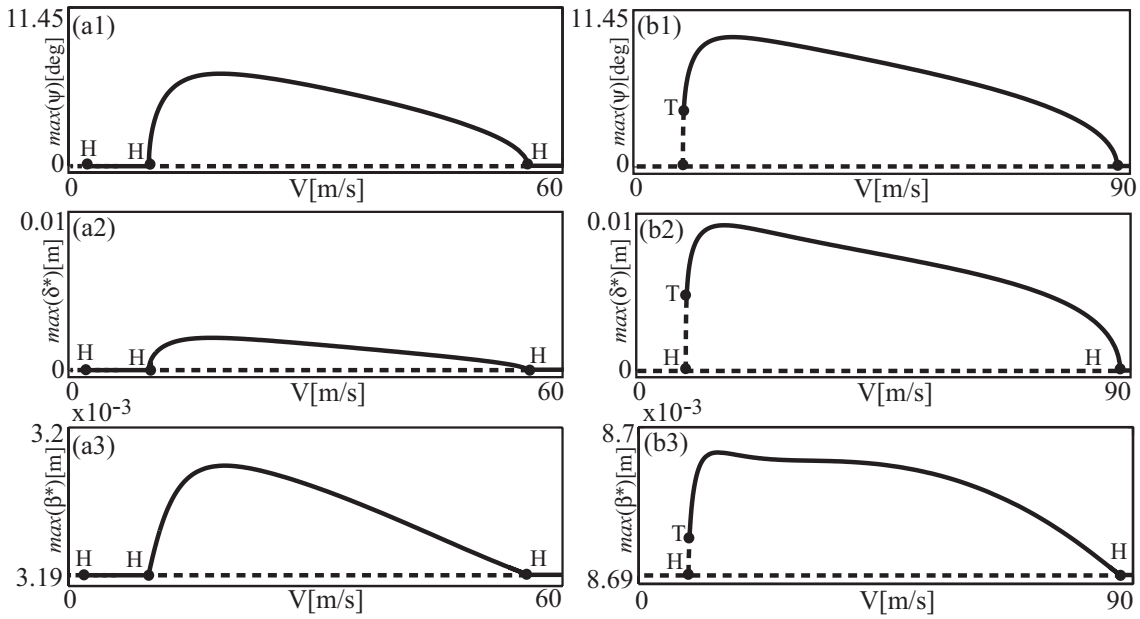

Figure 3. One-parameter continuation in V for $F_z = 60.0\,\mathrm{kN}$ (a) and $F_z = 162.0\,\mathrm{kN}$ (b); the individual panels show from top to bottom the maximum of the torsion angle ψ, the maximum of the lateral bending stroke δ^*, and the maximum of the longitudinal bending stroke β^*; stable parts of branches are drawn as solid curves, while unstable parts are dashed, with Hopf bifurcations labeled H and torus bifurcations labeled T.

in these panels correspond to a transient quasiperiodic behaviour in the vicinity of a torus bifurcation.[11,12] Depending on the distance from the torus bifurcation, the transient behaviour may last anywhere between a few tens of seconds to hundreds of seconds. In a situation such as take-off or landing, where the velocities change quite rapidly, such transient behaviour plays an important role in the observed dynamics.

An important conclusion from Fig. 2 is that the longitudinal mode does not appear to contribute to the landing gear dynamics. Even though we considered three qualitatively different types of shimmy oscillations, the longitudinal mode is excited only very weakly, oscillates with a negligible amplitude, and does not influence either the torsional or the lateral mode.

III.B. Shimmy oscillations as a function of forward velocity V

We now investigate the role of the longitudinal bending mode for the nose gear dynamics as described by Eqs. (4)–(7) over the range of 0–110 m/s of the forward velocity V for two fixed values of the downward force. Specifically, we perform a numerical continuation study of the equilibrium and bifurcating shimmy oscillations and their stability for the light and the heavy cases $F_z = 60$ kN and $F_z = 162$ kN. Note that this choice of F_z means that the examples of shimmy oscillations shown in Fig. 2 are covered by the one-parameter bifurcation diagrams presented here.

Figure 3 shows the resulting branches of solutions of two continuation runs in V for $F_z = 60$ kN and $F_z = 162$ kN. For each case, three panels show the maximum amplitude of the torsion angle ψ, of the lateral stroke δ^*, and of the longitudinal stroke β^*, respectively. Notice again the difference in scale between δ^* and β^*. The equilibrium solution of the gear, which corresponds to the desired straight-line motion, is represented by the straight line with zero amplitude in the panels. In both cases we find a single branch of shimmy oscillations with nonzero amplitudes of the modes. The equilibrium and the shimmy oscillations may be stable (solid curves) or unstable (dashed curves). Note that the straight-line motion may be stable for low and high velocities V for a given range of downward force F_z. Stability changes at bifurcation points, such as the Hopf bifurcation at which the shimmy oscillations are born. We also find changes of stability at torus bifurcations of shimmy oscillations; this means that a second frequency becomes involved in the gear motion.

Figure 3(a) shows a low loading case for $F_z = 60$ kN. Here, even though the straight-line equilibrium is unstable for very low velocities, it becomes stable in a Hopf bifurcation corresponding to the lateral mode and remains stable for the velocity range 2–9 m/s. As the velocity increases further, the stability of the stable

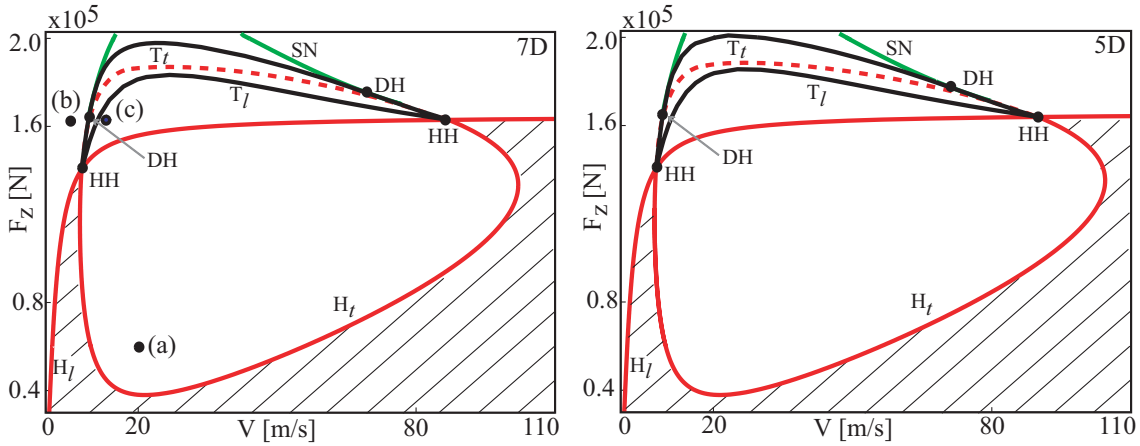

Figure 4. Two-parameter bifurcation diagram in the (V, F_z)-plane of Eqs. (4)–(7) consisting of curves of Hopf bifurcations, saddle-node of limit cycle bifurcations and torus bifurcations. In the left panel the longitudinal bending mode is active, and the right panel is for $\beta \equiv 0$, that is, for the model without longitudinal bending. The Hopf bifurcation curve H_t of the torsional mode forms an isola and changes criticality at two degenerate Hopf points DH (the dashed part is subcritical); it interacts with the Hopf bifurcation curve H_l of the lateral mode in two double Hopf points HH. In both panels, the shading represents the parameter region where the straight-line equilibrium is stable. The points (a), (b) and (c) in the left panel indicate the parameter values used in Fig. 2.

equilibrium is lost in a Hopf bifurcation H at $V \approx 9.8$ m/s. This Hopf bifurcation is supercritical, and it gives rise to stable periodic shimmy oscillations. The relative maximal amplitudes show that this type of shimmy oscillations is dominated by the torsional mode. Its maximal amplitude initially grows with V but decreases again above $V \approx 20$ m/s [Fig. 3(a1)]. The lateral frequency effectively remains dormant [Fig. 3(a2)] and the longitudinal motion is relatively small [Fig. 3(a3)], which indeed agrees with the dynamics in Fig. 2(a1)-(a5). The branch of stable torsional shimmy oscillations reduces to zero amplitude at $V \approx 55.8$ m/s in a third Hopf bifurcation H. Beyond this bifurcation point the straight-line equilibrium is stable and we do not see shimmy oscillations.

Figure 3(b) shows some marked differences for the higher loading case of $F_z = 162$ kN. Again, the straight-line equilibrium, which is already unstable, undergoes a stability change via a supercritical Hopf bifurcation H, now at $V \approx 9.2$ m/s. However, now the unstable shimmy oscillation that is born at the Hopf bifurcation quickly changes stability in a torus bifurcation T, which results in stable shimmy oscillations dominated by the torsional mode. The maximal amplitudes of the shimmy oscillations initially grow with V but then decrease again. Notice that the maximum amplitude of the torsional mode is now about 10 degrees. It is reached around $V \approx 16$ m/s, after which it decreases substantially [Fig. 3(b1)]; this is mirrored on a much smaller scale by the longitudinal mode [Fig. 3(b3)]. The maximum amplitude of the lateral mode of about 10 cm is also attained at $V \approx 16$ m/s [Fig. 3(b2)]. The branch of stable shimmy oscillations disappears at $V \approx 88.2$ m/s in a second Hopf bifurcation H. We remark that in the unstable region before the torus bifurcation the system jumps to stable pure lateral shimmy oscillations as shown in Fig. 2(b1)-(b5).

One of the main features of the one-parameter bifurcation diagrams in Fig. 3 is the negligible size of the longitudinal oscillations. Throughout the entire V-range, and for both loading cases, the longitudinal stroke β^* is at least two orders of magnitude smaller than the lateral stroke, never exceeding 0.1 mm. This forms evidence that the longitudinal motion β is insignificant for the landing gear dynamics for a free rolling nose landing gear.

III.C. Bifurcation diagram in the (V, F_z)-plane

We now consider the role of the longitudinal mode for the dynamics of the nose landing gear over the entire relevant range of the two main operational parameters V and F_z. To this end, we show in Fig. 4 the two-parameter bifurcation diagram in the (V, F_z)-plane of the seven-dimensional Eqs. (4)–(7) and of the five-dimensional model where $\beta \equiv 0$, both computed with the package AUTO for the parameter values in Table 1.

Figure 4(left) is the two-parameter bifurcation diagram for the seven-dimensional model (4)–(7), which includes the longitudinal degree of freedom β. It provides a global summary of the dynamics of this model

by presenting the locations of the main bifurcations. Specifically, we show the locations of Hopf bifurcations, saddle-node bifurcations and torus bifurcations. Along the curve H_t one finds Hopf bifurcations of the torsional mode, meaning that the bifurcating shimmy oscillations are dominated by the torsional component. The curve H_t forms an isola (closed curve); the solid part of the curve H_t corresponds to supercritical Hopf bifurcations, in which stable shimmy oscillations are born if the equilibrium before the bifurcation is stable, while the dashed part of H_t corresponds to subcritical Hopf bifurcations where unstable shimmy oscillations bifurcate. The transition between the super- and subcritical parts of H_t occurs at two special points DH that are known as degenerate Hopf points.[11,12] Each of these DH points is the starting point of a curve SN of saddle-node bifurcations. There is also a curve H_l of Hopf bifurcations of the lateral bending mode. It intersects the torsional Hopf curve H_t in two points HH that are known as double-Hopf points. As predicted by bifurcation theory,[11,12] we find that locally two curves of torus bifurcations emanate from each of the HH points. There are two main torus curves in Fig. 4(left): along T_t one finds torus bifurcations of the torsional shimmy oscillations born at H_t, and along T_l one finds torus bifurcations of the lateral shimmy oscillations born at H_l. Note that the curves T_l and T_t both connect the two codimension-two HH points.

Overall, the bifurcation curves in Fig. 4(left) organize the (V, F_z)-plane into regions with different types of dynamics. Specifically, the shaded region represents parameter values for which the straight-line equilibrium is stable, that is, there are no shimmy oscillations. Different regions bounded by the bifurcation curves correspond to different types of dynamics. Specifically, the three different types (a)-(c) of shimmy oscillations from Fig. 2 can be identified in Fig. 4(left). In the region including the point (a), the torsional mode is dominant; in the region including the point (b), shimmy oscillations are dominated by the lateral mode, and in the region including the point (c), one may observe coupling between the torsional and lateral modes. Note further that the one-parameter bifurcation diagrams in Figure 3(a) and (b) correspond to horizontal cross sections of Fig. 4(left) at $F_z = 60$ kN and $F_z = 162$ kN, respectively. The different bifurcations that are encountered as the forward velocity V is changed are readily identified.

Figure 4(right) shows the two-parameter bifurcation diagram for the five-dimensional model without inclusion of the longitudinal degree of freedom β. The agreement with the bifurcation diagram in Fig. 4(left) is immediate. The corresponding bifurcation curves differ by less than 1% across the entire (V, F_z)-plane. The only minor difference between the left and the right panels is the fact that the isola of H_t encloses a slightly smaller area of the (V, F_z)-plane in Fig. 4(left). This is due to the increase in the effective rake angle $(\phi + \beta)$ in the presence of the longitudinal mode β. Overall, the excellent agreement of the two bifurcation diagrams constitutes conclusive evidence over the entire range of the operating parameters V and F_z that the longitudinal motion β does indeed not influence the landing gear dynamics in any significant way.

IV. Effects of torsional damping

We now perform a study of how the torsional damping c_ψ influences the bifurcation diagram in the (V, F_z)-plane. Here, we make use of the fact that the longitudinal mode β does not play a significant role in the dynamics of the landing gear, so that it suffices to consider the five-dimensional model where $\beta \equiv 0$. The damping c_ψ models the overall damping characteristics in the torsional mode of nose landing gear. Specifically, it includes the damping associated with an extra torsional or shimmy damper that is often installed on landing gears to curtail torsional oscillations. The disadvantage of shimmy dampers is that they increase the mass of the landing gear, contributing to the overall weight of the aircraft. Hence, a study of the effects of torsional damping on shimmy oscillations is important for evaluation and design of a landing gear.

Figure 5 shows two-parameter bifurcation diagrams for the torsional damping values $c_\psi = 150$ N m s rad^{-1} in panel (a) and $c_\psi = 70$ N m s rad^{-1} in panel (b), where all other parameters are as shown in Table 1. The two panels of Fig. 5 correspond to larger and smaller values of c_ψ than that of 110 N m s rad^{-1} given in Table 1 and used in Fig. 4. It is quite evident from Figs. 5(a),(b) and Fig. 4(right) that, as torsional damping decreases, the torsional shimmy region enclosed by the curve H_t becomes significantly larger. In contrast, decreasing c_ψ reduces the region corresponding to lateral shimmy, but this is a small effect. This reduction is due to the transfer of energy from the lateral bending mode into the torsional mode.

We now investigate how the region (the isola) corresponding to torsional oscillations varies over a wider range of c_ψ values. To this end we show in Fig. 6 the minimum and maximum of the velocity along H_t as a function of c_ψ. The corresponding values $\mathrm{H}_t^{\min}$ and $\mathrm{H}_t^{\max}$ were computed for the seven different values of c_ψ that are marked as dots in Fig. 6. This data was then used to obtain the solid curves by spline interpolation.

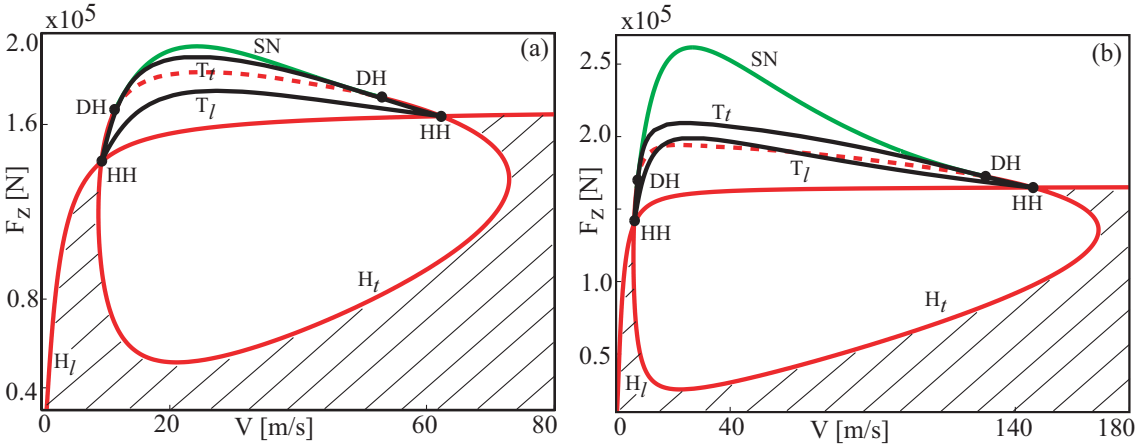

Figure 5. Panels (a) and (b) show the two-parameter bifurcation diagrams of Eqs. (4)–(7) in the (V, F_z)-plane with parameter values as in Fig. 4(b), but for $c_\psi = 150$ N m s rad^{-1} and $c_\psi = 70$ N m s rad^{-1} respectively.

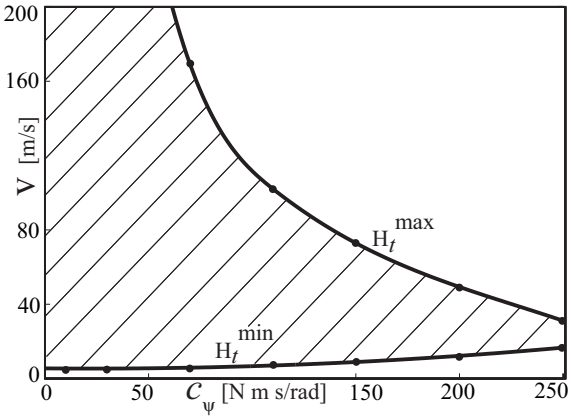

Figure 6. The left-most point $\mathrm{H}_t^{\min}$ and the right-most point $\mathrm{H}_t^{\max}$ of the Hopf bifurcation curve H_t as a function of c_ψ. The shaded region corresponds to the area in the two-parameter bifurcation diagrams where torsional oscillations can occur.

Torsional shimmy oscillations can occur in the shaded region bounded by the two interpolated curves. We observe that while a change in c_ψ has very little effect on $\mathrm{H}_t^{\min}$, it has a large effect on $\mathrm{H}_t^{\max}$. Specifically, for $c_\psi = 200$ N m s rad^{-1}, torsional oscillations can occur only between $V \approx 11$ m/s and $V \approx 50$ m/s. At a lower value of c_ψ, say $c_\psi = 100$ N m s rad^{-1}, on the other hand, torsional oscillations are born above $V \approx 7$ m/s and may be sustained for velocities greater than the average take-off velocity of a midsize passenger aircraft. As an extreme case we also calculate $\mathrm{H}_t^{\min}$ and $\mathrm{H}_t^{\max}$ for $c_\psi = 10$ N m s rad^{-1}, where $\mathrm{H}_t^{\max}$ is at $V \approx 1207$ m/s, which falls well outside the range of Fig. 6. A study in Thota *et al.*[14] found that $H_t^{\min}$ and $H_t^{\max}$ depend linearly on the rake angle ϕ. Such studies expand the existing knowledge of the parameter dependence of shimmy oscillations. In particular, they provide crucial sensitivity information that can assist in choosing optimal damping parameters over an entire operational range.

V. Conclusions

This work focused on the interaction of different vibrational modes in shimmy oscillations of the nose landing gear of a generic midsized passenger aircraft. Specifically, we developed a seven-dimensional model that includes torsional, lateral and longitudinal degrees of freedom. Time histories and frequency spectra, in conjunction with a numerical bifurcation analysis in the forward velocity and the vertical force on the gear, showed that the torsional and the lateral bending modes interact very strongly to give rise to different types of shimmy oscillations. By contrast, the longitudinal degree of freedom does not actively participate in any of the different possible types of shimmy oscillations.

The overall conclusion is that the longitudinal degree of freedom can safely be omitted in the analysis of nose landing gear shimmy. Hence, without a sacrifice in qualitative and quantitative accuracy, it is sufficient to work with a five-dimensional model. This reduction in dimensionality and complexity of the model is of practical interest because it allows for more extensive bifurcation studies of the landing gear system. In this way, even quite complicated dynamical scenarios can be investigated. As an example, we presented the investigation of the dependence of shimmy oscillations on torsional damping c_ψ. The analysis concluded that the choice of appropriate overall torsional damping is crucial in minimizing the velocity range in which torsional shimmy occurs. In the longer term, dynamical scenarios, including acceleration during take-off and braking after landing, could be considered. In this case, forward velocity and vertical force are not independent of each other and their relationship can be derived from flight test data. Furthermore, the study of a braking aircraft may require the inclusion of a vertical degree of freedom due to possible excitement of oleo (shock damper) dynamics.

VI. Acknowledgments

We thank Airbus for their financial and technical support of this research. We also thank Etienne Coetzee for sharing his technical insights.

References

[1]Baumann, J., "A Nonlinear model for landing gear shimmy with applications to the McDonnell Douglas G/A-18A", 81^{st} *Meeting of the AGARD Structures and Materials Panel*, AGARD-R-800, 1995.

[2]Besselink, I. J. M., "Shimmy of aircraft main landing gears", *Dissertation,* University of Delft, The Netherlands, 2000.

[3]Glaser, J., and Hrycko, G., "Landing gear shimmy - De Havilland's experience", 81^{st} *Meeting of the AGARD Structures and Materials Panel*, AGARD-R-800, 1995.

[4]Krabacher, W. E., "A Review of Aircraft Landing Gear Dynamics", 81^{st} *Meeting of the AGARD Structures and Materials Panel*, AGARD-R-800, 1995.

[5]Dengler, M., Goland, M., and Herrman, G., "A bibliographic survey of automobile and aircraft wheel shimmy," *Technical report, Midwest Research Institute,* Kansas city, MO, USA, 1951.

[6]Smiley, R. F., "Correlation, evaluation, and extension of linearized theories for tyre motion and wheel shimmy", NACA-1299, 1957.

[7]Pritchard, I. J., "An overview of landing gear dynamics", NASA/TM-1999-209143, 1999.

[8]Broulhiet, M. G., "La suspension de la direction de la voiture automobile - Shimmy et dandinement", *Bull. Soc. Ing. Civ.*, France, 78, 1925.

[9]von Schlippe, B., and Dietrich, R., "Shimmying of a pneumatic wheel", NACA-TM 1365, 1947.

[10]Somieski, G., "Shimmy analysis of a simple aircraft nose landing gear model using different mathematical methods", *Aerospace Science and Technology*, 1270-9638(8), 1997.

[11]Guckenheimer, J., and Holmes, P., "Nonlinear oscillations, dynamical systems and bifurcations of vector fields", Springer, New York, 1983.

[12]Kuznetsov, Yu. A.,"Elements of applied bifurcation theory", Springer, New York, 1995.

[13]Woerner, P., and Noel, O., "Influence of nonlinearity on the shimmy behaviour of landing gear", 81^{st} *Meeting of the AGARD Structures and Materials Panel*, AGARD-R-800, 1995.

[14]Thota, P., Krauskopf, B., and Lowenberg, M., "Interaction of torsion and lateral bending in aircraft nose landing gear shimmy, "*Nonlinear Dynamics*, (to appear), 2009.

[15]Pacejka, H. B., "Analysis of the shimmy phenomenon", *Proceedings of The Institute of Mechanical Engineers*, 180(2A)(10), 1965-66.

[16]Doedel, E. J., Champneys, A. R., Fairgrieve, T., Kuznetsov, Yu., Sandstede, B., and Wang, X., "AUTO 97 : Continuation and bifurcation software for ordinary differential equations", `http://indy.cs.concordia.ca/auto/`, May 2001.

[17]Doedel, E. J., "Notes on numerical analysis of nonlinear equations", in Krauskopf, B., Osinga, H. M., and Galán-Vioque, J., (eds.) *Numerical continuation methods for dynamical systems: path following and boundary value problems*, Springer-Verlag, pp. 1–49, 2007.

[18]Thota, P., Krauskopf, B. and Lowenberg, M., "Shimmy in a nonlinear model of an aircraft nose landing gear with nonzero rake angle", *Proceedings of European Nonlinear Oscillations Conference*, St. Petersburg, 2008.